Nuclear effects in high-p_T production of direct photons and neutral mesons

L. Apanasevich,[1,2] J. Bacigalupi,[3] W. Baker,[4] M. Begel,[2] S. Blusk,[5] C. Bromberg,[1] P. Chang,[6] B. Choudhary,[7] W. H. Chung,[5] L. de Barbaro,[2] W. DeSoi,[2] W. Długosz,[6] J. Dunlea,[2] E. Engels, Jr.,[5] G. Fanourakis,[2] T. Ferbel,[2] J. Ftacnik,[2] D. Garelick,[6] G. Ginther,[2] M. Glaubman,[6] P. Gutierrez,[8] K. Hartman,[9] J. Huston,[1] C. Johnstone,[4] V. Kapoor,[7] J. Kuehler,[8] C. Lirakis,[6] F. Lobkowicz,[2,*] P. Lukens,[4] J. Mansour,[2] A. Maul,[1] R. Miller,[1] B. Y. Oh,[9] G. Osborne,[2] D. Pellett,[3] E. Prebys,[2] R. Roser,[2] P. Shepard,[5] R. Shivpuri,[7] D. Skow,[4] P. Slattery,[2] L. Sorrell,[1] D. Striley,[6] W. Toothacker,[9,*] S. M. Tripathi,[3] N. Varelas,[2] D. Weerasundara,[5] J. J. Whitmore,[9] T. Yasuda,[6] C. Yosef,[1] M. Zieliński,[2] and V. Zutshi[7]

(Fermilab E706 Collaboration)

[1]*Michigan State University, East Lansing, Michigan 48824, USA*
[2]*University of Rochester, Rochester, New York 14627, USA*
[3]*University of California–Davis, Davis, California 95616, USA*
[4]*Fermi National Accelerator Laboratory, Batavia, Illinois 60510, USA*
[5]*University of Pittsburgh, Pittsburgh, Pennsylvania 15260, USA*
[6]*Northeastern University, Boston, Massachusetts 02115, USA*
[7]*University of Delhi, Delhi, India 110007*
[8]*University of Oklahoma, Norman, Oklahoma 73019, USA*
[9]*Pennsylvania State University, University Park, Pennsylvania 16802, USA*
(Received 31 May 2005; published 11 August 2005)

We present results on the production of direct photons, π^0, and η mesons on nuclear targets at large transverse momenta (p_T). The data are from 530 and 800 GeV/c proton beams and 515 GeV/c π^- beams incident upon copper and beryllium targets that span the kinematic range of $1.0 < p_T \lesssim 10$ GeV/c at central rapidities.

DOI: 10.1103/PhysRevD.72.032003 PACS numbers: 13.85.Qk, 12.38.Qk

I. INTRODUCTION

The study of inclusive particle production at large transverse momenta (p_T) has yielded valuable information about perturbative quantum chromodynamics, parton distribution functions, and fragmentation functions of partons [1–5]. The use of nuclear targets provides, in addition, information on parton and hadron rescattering and explores the time evolution of the collision. Since the discovery of the nuclear enhancement of high-p_T single-particle production [6–8], a large body of data has been accumulated to investigate nuclear-target effects in a wide variety of production processes, including those yielding single hadrons, dihadron pairs, Drell-Yan pairs, two-jet systems, and heavy flavors. Recent results from the Relativistic Heavy Ion Collider (RHIC) program [9–12], in particular, have highlighted the differences between initial and final-state effects in the nuclear environment. Many approaches have been developed to explain these data, which have included models for multiple scattering, Fermi motion, modification of parton densities in the nuclear medium, quantum chromodynamic higher-twist contributions, and new states of matter.

We present the results of a high-statistics study of nuclear effects in the inclusive production of direct photons, π^0 and η mesons at large p_T using data from Fermilab experiment E706, and compare the results to predictions of a phenomenological model of nuclear effects [13].

II. APPARATUS

A. Meson West spectrometer

Fermilab E706 was a fixed-target experiment designed to measure the production of direct photons, neutral mesons, and associated particles at high p_T [14–19]. The apparatus included a charged-particle spectrometer and a large liquid-argon calorimeter, as described below. Additional information about the Meson West spectrometer can be found in earlier papers [18,20]. The physical layout of the Meson West spectrometer is shown in Fig. 1.

This paper reports on data from the two primary data runs of the experiment. During the 1990 run, the target consisted of two 0.8 mm thick copper foils followed by two pieces of beryllium (Fig. 2, top). The upstream piece of beryllium was 3.7 cm long, while the length of the downstream piece was 1.1 cm. In the 1991–1992 run, the target consisted of two 0.8 mm thick copper foils immediately upstream of a liquid hydrogen target [21], followed by a 2.54 cm long beryllium cylinder (Fig. 2, bottom). The liquid hydrogen was contained in a 15.3 cm long Mylar flask, which was supported in an evacuated volume with beryllium windows at each end (2.5 mm thickness upstream and 2.8 mm thickness downstream). The target material is detailed in Table I.

*Deceased.

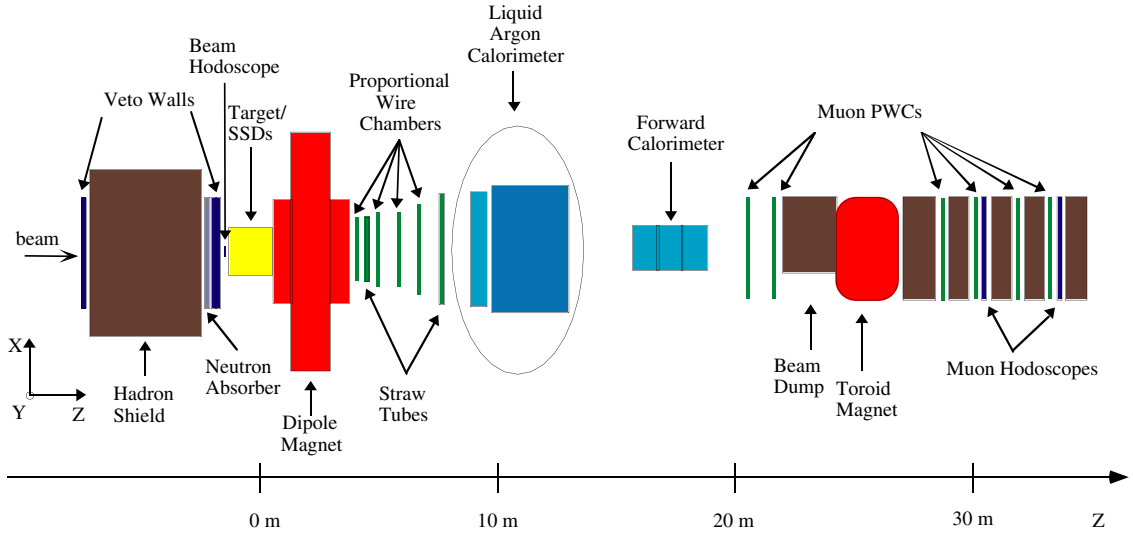

FIG. 1 (color online). Schematic view of the Fermilab Meson West spectrometer, as configured for the 1990 fixed-target run.

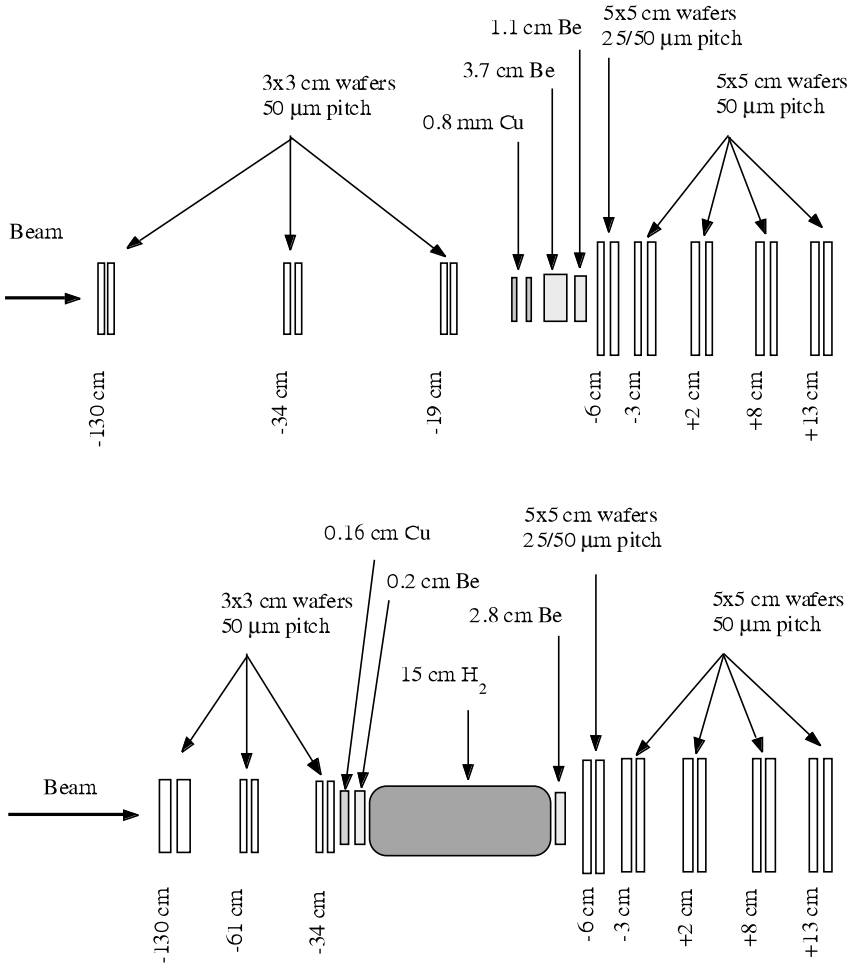

FIG. 2. Target configuration during the 1990 (top) and 1991–1992 (bottom) fixed-target runs.

TABLE I. Target fiducial lengths, densities, and number of interaction lengths for each beam and target configuration. The interaction lengths for the nuclear targets were obtained from Ref. [22]; for the H_2 target they were obtained from Ref. [23]. $\sqrt{s}$ is calculated for the beam-nucleon system.

Target layout	Beam (GeV/c)	$\sqrt{s}$ (GeV)	Target	Fiducial length (cm)	Measured density (g/cm^3)	Interaction length (g/cm^2)
1990	515 π^-	31.1	Be	4.829	1.848	0.086
			Cu	0.156	8.810	0.008
	515 π^-	31.1				0.055
	530 p	31.6	Be	3.070	1.855	0.073
	800 p	38.8				0.074
	515 π^-	31.1				0.008
1991–1992	530 p	31.6	Cu	0.156	8.810	0.010
	800 p	38.8				0.010
	515 π^-	31.1				0.004
	530 p	31.6	H_2	14.500	0.0705	0.020
	800 p	38.8				0.021

The charged-particle spectrometer consisted of silicon microstrip detectors (SSDs) in the target region and multiwire proportional chambers (PWCs) and straw tube drift chambers (STDCs) downstream of a large-aperture analysis magnet [18]. Six 3×3 cm^2 SSD planes were located upstream of the target region and used to reconstruct beam tracks. Two hybrid 5×5 cm^2 SSD planes (25 μm pitch strips in the central 1 cm, 50 μm beyond) were located downstream of the target region. These were followed by eight 5×5 cm^2 SSD planes of 50 μm pitch. The analysis dipole magnet imparted a 0.45 GeV/c p_T impulse in the horizontal plane to charged particles. Downstream track segments were measured by means of four stations of four views ($XYUV$) of 2.54 mm pitch PWCs and two stations of eight ($4X4Y$) layers of STDCs with tube diameters 1.03 cm (upstream station) and 1.59 cm (downstream station) [24].

Photons were detected in a large, lead and liquid-argon sampling electromagnetic calorimeter (EMLAC), located 9 m downstream of the target [20]. The EMLAC had a cylindrical geometry with an inner radius of 20 cm and an outer radius of 160 cm. The calorimeter had 33 longitudinal cells read out in two sections: an 11 cell front section (8.5 radiation lengths) and a 22 cell back section (18 radiation lengths). Each longitudinal cell consisted of a 2 mm thick lead cathode (the first cathode was constructed of aluminum), a double-sided copper-clad G-10 radial (R) anode board, a second 2 mm thick lead cathode, and a double-sided copper-clad G-10 azimuthal (Φ) anode board. The 2.5 mm gaps between these layers were filled with liquid argon. The physical layout is illustrated in Fig. 3.

The EMLAC readout was subdivided azimuthally into octants, each consisting of interleaved, finely segmented, radial and azimuthal views. This segmentation was realized by cutting the copper cladding on the anode boards to form either radial or azimuthal strips. Signals from corresponding strips from all R (or Φ) anode boards in the front (or back) section of a given octant were jumpered together. The copper cladding on the radial anode boards was cut into concentric strips centered on the nominal beam axis. The width of the strips on the first R board was 5.5 mm. The width of the strips on the following R boards increased slightly so that the radial geometry was projective relative to the target region. The azimuthal strips were split at a radius of 40 cm into inner and outer segments; each inner strip subtended an azimuthal angle of $\pi/192$ radians, while outer strips covered $\pi/384$ radians.

The spectrometer was located at the end of the Meson West beam line. The design of the beam line, primary

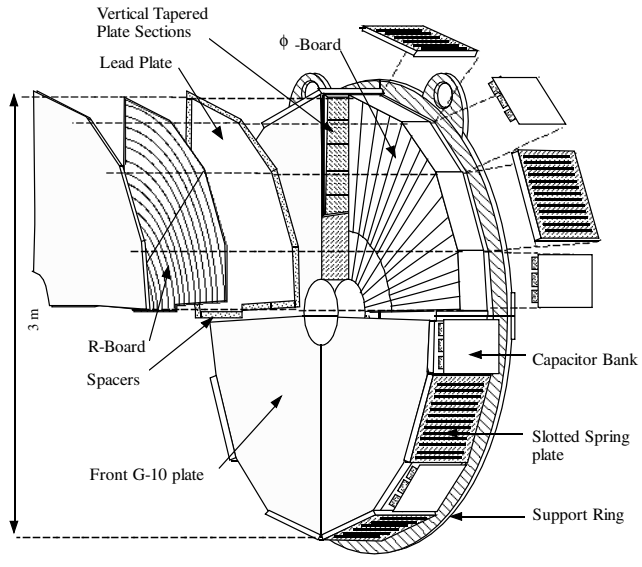

FIG. 3. A drawing of the liquid-argon electromagnetic calorimeter with some components pulled away in one quadrant to reveal a view of the internal details.

target, and primary beam dump were intended to minimize the rate of beam-halo muons incident upon the spectrometer. The beam line was capable of transporting either a primary (800 GeV/c) proton beam or unseparated secondary particle beams of either polarity to the experimental hall. The beam line Čerenkov detector was used to identify the secondary beam particles [25]. This 43.4 m long helium-filled counter was located 100 m upstream of the experimental target. The positive secondary beam with mean momentum of 530 GeV/c was 97% protons. The negative secondary beam with mean momentum of 515 GeV/c was 99% pions.

At the end of the beam line was a 4.7 m long stack of steel surrounding the beam pipe and shadowing the EMLAC to absorb off-axis hadrons. A water tank was placed at the downstream end of this hadron shield to absorb low-energy neutrons. Surrounding the hadron shield and neutron absorber were walls of scintillation counters (VW) to identify penetrating muons. There was one wall at the upstream end and two walls at the downstream end of the hadron absorber during the 1990 run. An additional wall was added to the upstream end of the hadron absorber prior to the 1991–1992 run.

B. Trigger

The E706 trigger selected interactions yielding high-p_T showers in the EMLAC. The selection process involved several stages: beam and interaction definitions, a pretrigger, and high-p_T trigger requirements [15,18,26]. A scintillator hodoscope, located 2 m upstream of the target region, was used to detect beam particles, and reject interactions with more than one spatially isolated incident particle. Additional scintillator with a 1 cm diameter central hole was located just downstream of the beam hodoscope, and served to reject interactions initiated by particles in the beam halo [27]. Two pairs of scintillator counters, mounted on the dipole analysis magnet, were used to identify interactions in the target. To minimize potential confusion in the EMLAC due to out-of-time interactions, a filter was employed to reject interactions that occurred within 60 ns of one another.

For those interactions that satisfied the beam and interaction requirements, the p_T deposited in various regions of the EMLAC was evaluated by weighting the energy signals from the EMLAC R-channel amplifier fast outputs by a factor proportional to $\sin\theta_i$, where θ_i was the polar angle between the ith strip and the nominal beam axis. The PRETRIGGER HI requirement for a given octant was satisfied when the p_T detected in either the inner 128 R channels or the outer R channels of that octant was greater than a threshold value. A pretrigger signal was issued only when there was no evidence in that octant of substantial noise, significant p_T attributable to an earlier interaction, or incident beam-halo muon detected by the VW.

Localized trigger groups were formed for each octant by clustering the R-channel fast outputs into 32 groups of 8 channels. Each adjacent pair of 8 channel groups formed a group of 16 strips. If the p_T detected in any of these groups of 16 was above a specified high (or low) threshold, then a LOCAL HI (or LOCAL LO) signal was generated for that octant. A SINGLE LOCAL HI (or SINGLE LOCAL LO) trigger was generated if a LOCAL HI (or LOCAL LO) signal was generated in coincidence with the PRETRIGGER HI in the same octant.

Trigger decisions were also made based upon global energy depositions within an octant. A GLOBAL LO signal was generated if the total p_T in an octant exceeded a threshold value. The LOCAL ⊗ GLOBAL LO trigger required a coincidence of the PRETRIGGER HI signal with GLOBAL LO and LOCAL LO signals from the same octant. The LOCAL LO requirement was included to suppress spurious global triggers due to coherent noise in the EMLAC.

The SINGLE LOCAL LO and LOCAL ⊗ GLOBAL LO triggers were prescaled to keep them from dominating the trigger rate. Prescaled samples of beam, interaction, and pretrigger events were also recorded.

III. ANALYSIS METHODS

Data samples contributing to this analysis represent an integrated luminosity of 1.6 (6.8) pb^{-1} and 1.6 (6.5) pb^{-1} for 530 and 800 GeV/c pCu (pBe) interactions, respectively, as well as 0.3 (1.4) pb^{-1} for 515 GeV/c π^-Cu (π^-Be) interactions. These samples were accumulated during the 1991–1992 run. Results reported in this paper also use 0.9 (6.1) pb^{-1} of π^-Cu (π^-Be) data recorded during the 1990 run. The following subsections describe the analysis procedures and methods used to correct the data for losses from inefficiencies and selection biases. Additional details can be found in our previous papers [15–18,20].

A. Charged-particle reconstruction

The two major aspects of the analysis procedure involved charged-particle and calorimeter-shower reconstruction (discussed in Sec. III B). The charged-track reconstruction algorithm produced track segments upstream of the magnet using information from the SSDs, and downstream of the magnet using information from the PWCs and STDCs. These track segments were projected to the center of the magnet and linked to form final tracks whose calculated charges and momenta were used for the physics analysis. The charged-track reconstruction is described in more detail elsewhere [18,28]. The primary vertex reconstruction is described in Sec. III E.

B. Calorimeter-shower reconstruction

The readout of each EMLAC quadrant was divided into four regions: left and right R, and inner and outer Φ. Strip

energies from clusters in each region were fit to the shape of an electromagnetic shower determined from detailed Monte Carlo simulations and isolated-shower data. These fits were used to evaluate the positions and energies of the peaks in each region. Shower positions and energies were obtained by correlating peaks of approximately the same energy in the R and Φ regions within the same half octant. More complex algorithms were used to handle configurations with showers spanning multiple regions. The EMLAC readout was also subdivided longitudinally into front and back sections. This segmentation provided discrimination between showers generated by electromagnetically or hadronically interacting particles. Photons were defined as showers with at least 20% of the shower energy deposited in the front part of EMLAC, to reduce the backgrounds due to showers from hadronic interactions. Losses of photons due to this requirement were $\approx 2\%$. A detailed event simulation was employed to correct for this and other effects including reconstruction smearing and losses. An expanded discussion of the EMLAC reconstruction procedures and performance can be found elsewhere [20].

C. Meson signals

For this study, π^0 and η mesons were reconstructed via their $\gamma\gamma$ decay modes. Only those $\gamma\gamma$ combinations with energy asymmetry $A_{\gamma\gamma} = |E_{\gamma_1} - E_{\gamma_2}|/(E_{\gamma_1} + E_{\gamma_2}) < 0.75$ were considered to reduce uncertainties due to low-energy photons. The meson signals have been corrected for losses due to the energy asymmetry cut and the branching fractions for the $\gamma\gamma$ decay modes [29].

Photons were required to be reconstructed within the fiducial region of the EMLAC to exclude areas with reduced sensitivity. In addition, $\gamma\gamma$ combinations were restricted to the same octant to simplify the trigger analysis. A simple ray-tracing Monte Carlo program was employed to determine the correction for these fiducial requirements.

The correction for losses due to the conversion of photons into e^+e^- pairs was evaluated by projecting each reconstructed photon from the primary vertex to the reconstructed position in the EMLAC. The radiation length of material traversed, up to the analysis magnet, was evaluated based upon detailed detector descriptions. The photon conversion probability was evaluated and used to account for conversion losses. The average correction for conversion losses was 1.09 per photon for the Be target in the 1990 run (1.08 in 1991–1992 run) and 1.19 per photon for the Cu target (1.16 in 1991–1992 run).

D. Detector simulation

The Meson West spectrometer was modeled with a detailed GEANT [30] simulation (DGS). A preprocessor was used to convert GEANT information into the simulated hits and strip energies associated with the various detectors. The preprocessor simulated hardware effects, such as channel noise and gain variations. Monte Carlo events were then processed through the same reconstruction software used for the analysis of the data. This technique accounted for inefficiencies and biases in the reconstruction algorithms. Reconstruction inefficiencies were relatively small over most of the kinematic range. More information on the detailed simulation of the Meson West spectrometer can be found elsewhere [15,17,31].

As inputs to the GEANT simulation, we employed single-particle distributions, reconstructed data events, and HERWIG-generated [32] events. The HERWIG-generated π^0, η, and direct-photon spectra were weighted in p_T and rapidity to our measured results in an iterative fashion so that the final corrections were based on the data distributions rather than on the behavior of the physics generator. Figure 4 shows the $\gamma\gamma$ mass spectra in the π^0 and η mass regions in comparison to the DGS results for the π^-Cu data at 515 GeV/c, and Fig. 5 shows an analogous plot for our higher statistics pBe data at 530 GeV/c. In addition to providing evidence that the DGS simulated the EMLAC resolution well, the agreement between the levels of combinatorial background indicates that the DGS also provided a reasonable simulation of the underlying event structure. Since the DGS was tuned using our higher statistics Be data, Figs. 6 and 7 also show the level of agreement achieved for this target. Figure 6 shows a comparison between the DGS and the data for the sideband-subtracted energy asymmetry distribution for photons from π^0 decays. This figure illustrates that the simulation accurately describes the losses of low-energy photons.

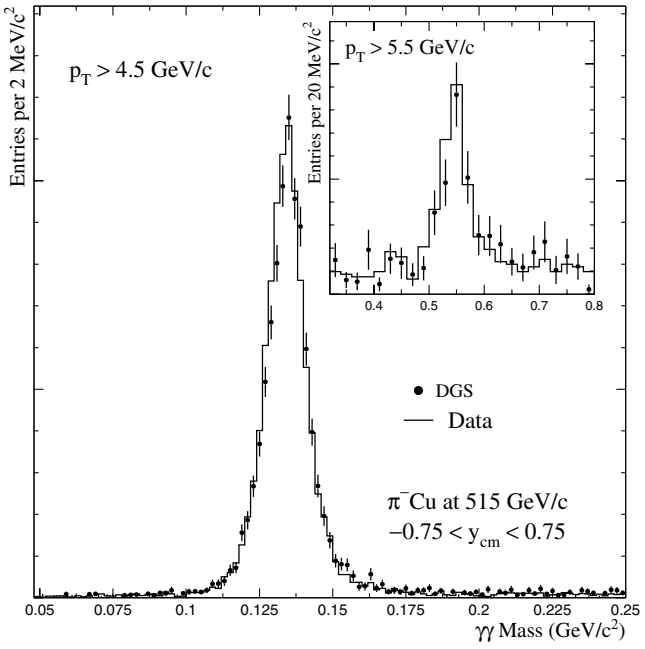

FIG. 4. Comparison between data (histogram) and the detailed Monte Carlo simulation (•) for 515 GeV/c π^- beam on Cu for $\gamma\gamma$ combinations in the π^0 and η mass regions.

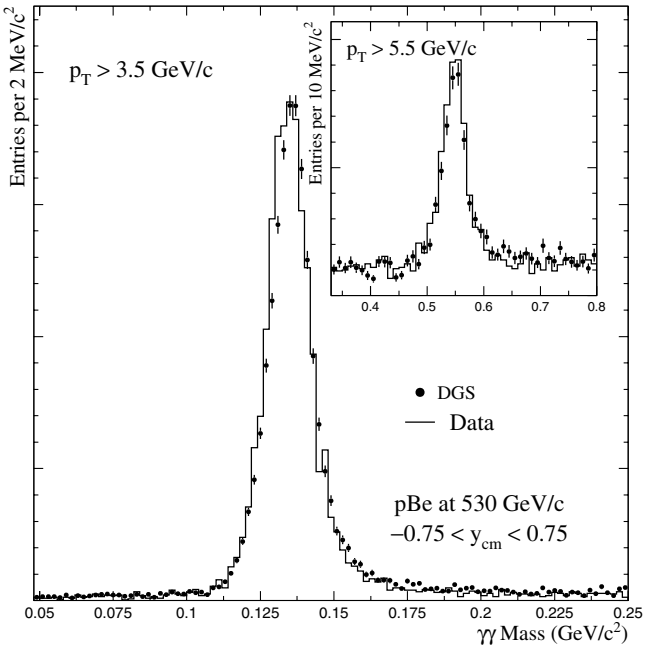

FIG. 5. Comparison between data (histogram) and the detailed Monte Carlo simulation (•) for 530 GeV/c proton beam on Be for $\gamma\gamma$ combinations in the π^0 and η mass regions.

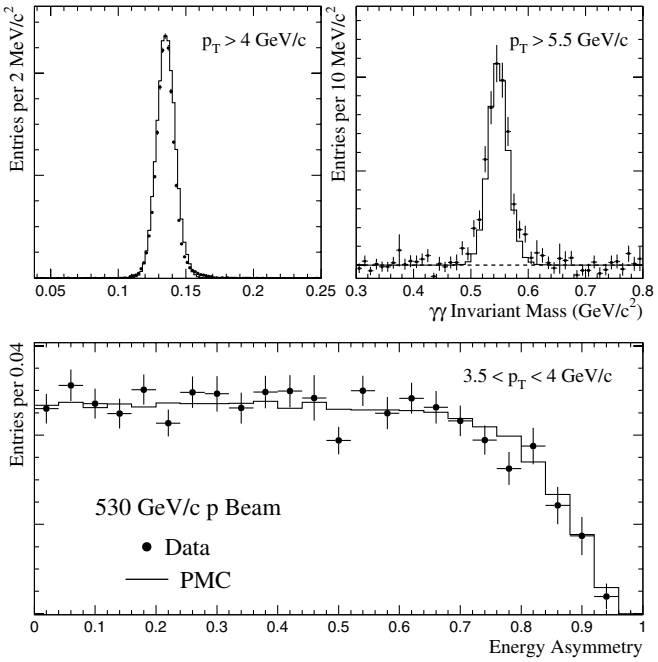

FIG. 7. Comparison between data (•) and the parametrized Monte Carlo (histogram) from the 530 GeV/c proton beam sample: (top) $\gamma\gamma$ combinations in the π^0 and η mass regions; (bottom) asymmetry in energy for photons from π^0 mesons. The combinatorial background in the data has been removed from this comparison through a simple subtraction. The distributions have been normalized to the same area.

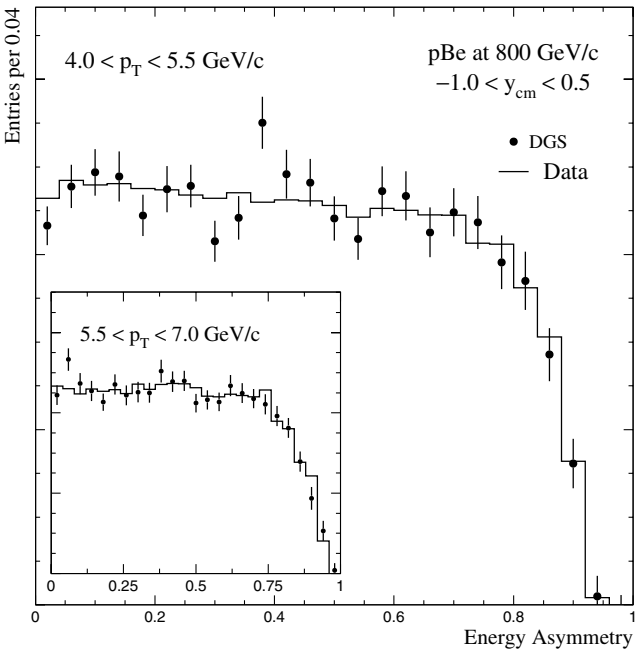

FIG. 6. Comparison of $A_{\gamma\gamma}$, the energy asymmetry distribution for photons from π^0 decays, in data (histogram) and the detailed Monte Carlo simulation (•) for the 800 GeV/c proton beam sample. Shown are the comparisons for two p_T intervals, $4.0 < p_T < 5.5$ GeV/c and $5.5 < p_T < 7.0$ GeV/c.

A second Monte Carlo simulation of the detector (PMC) was used to cross-check the detailed simulation and for studies that required large statistics. This simulation employed parametrizations of physics cross sections and detector responses [17,31,33]. The inclusive π^0 and direct-photon cross sections were parametrized as two-dimensional surfaces in p_T and rapidity [31]. The η, ω, and η' cross sections were parametrized using the measured η/π^0 [15,16], ω/π^0 [19], and η'/η [1,34] ratios. Generated mesons were decayed into final-state particles; photons were smeared for energy and position resolution [20]. A vertex was generated in the simulated target for every event. Photons were allowed to convert into e^+e^- pairs; the energy of the resulting electrons was reduced using the GEANT function for bremsstrahlung radiation. Electron four-vectors were smeared for multiple scattering in the target and the resolution of the tracking system and adjusted for the magnet impulse. Figure 7 displays a comparison between the PMC and the data in the π^0 and η mass regions and for the π^0 energy asymmetry. The PMC provides an adequate characterization of the data.

E. Vertex reconstruction

The location of the primary interaction vertex was reconstructed using charged-particle tracks. Vertices were

identified by means of an impact-parameter minimization technique [28]. A χ^2 was defined for a given vertex position using the impact parameters of the reconstructed tracks and their projection uncertainties. The vertex position was found by minimizing this χ^2. Vertices were found in X and Y independently and correlated based on the difference in their positions along the nominal beam direction (Z axis). The Z position of the matched vertex was the weighted average of the Z positions found in X and Y. The reconstructed vertex positions are presented in Fig. 8 as functions of Z for the two target configurations. The beryllium, copper, and hydrogen targets are clearly visible, as are the SSDs and related support structures. The average resolution for the Z location of the interaction vertex was $\approx 300\ \mu$m [18,28].

The relative heights of the Cu and Be targets shown in Fig. 8 vary as a function of p_T. This is clearly evident in Fig. 9, which compares two π^0 samples: one acquired using the highly prescaled INTERACTION trigger, and the other using the SINGLE LOCAL HI trigger. The INTERACTION triggered events are typically minimum-bias in character with low-p_T π^0's. The number of primary vertices scales as $\approx A^{2/3}$, where A is the atomic weight of the target. The SINGLE LOCAL HI triggers are typically caused by hard scatters that produce high-p_T π^0's. The number of primary vertices in these events scale as $\approx A^1$.

The DGS was used for detailed studies of the vertex reconstruction. The transverse positions of vertices were chosen according to beam profiles observed in the data.

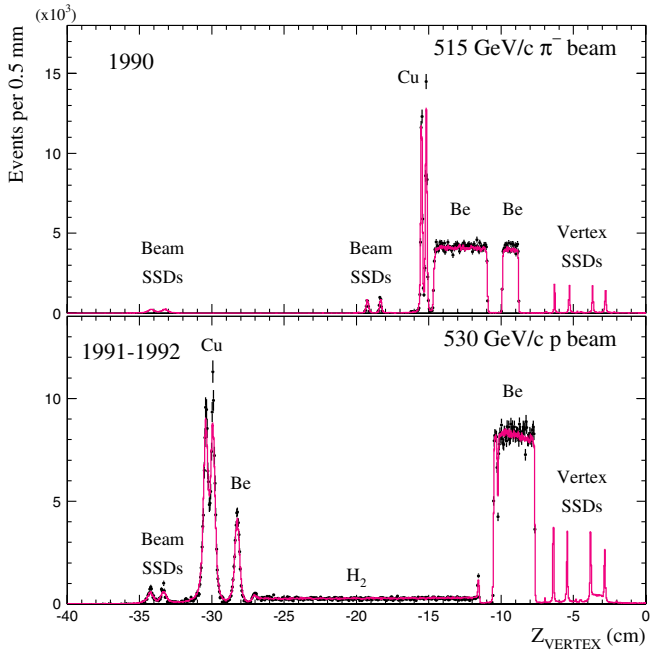

FIG. 8 (color online). Z positions of primary vertices in the detailed Monte Carlo simulation (•) and the data (histogram) for events containing a π^0 candidate with $p_T > 4$ GeV/c.

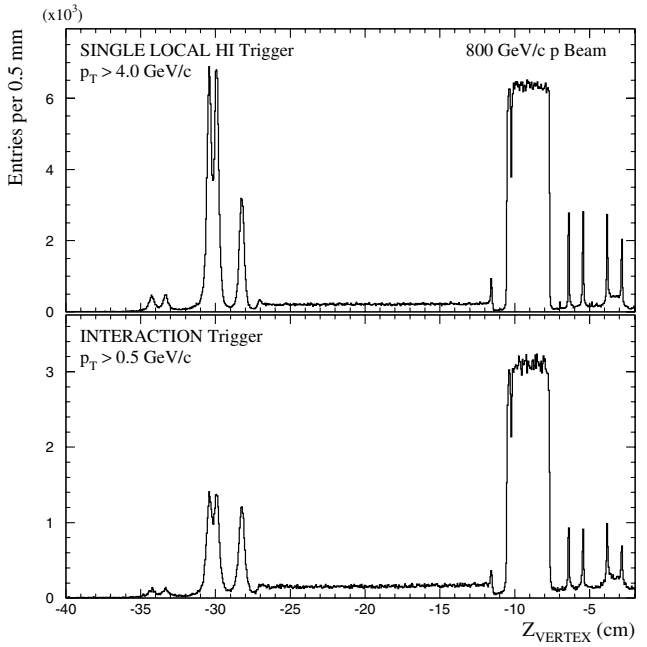

FIG. 9. Z positions of primary vertices for events containing π^0 candidates with $p_T > 4.0$ GeV/c acquired using the SINGLE LOCAL HI trigger (top) and for events containing π^0 candidates with $p_T > 0.5$ GeV/c acquired using the INTERACTION trigger (bottom).

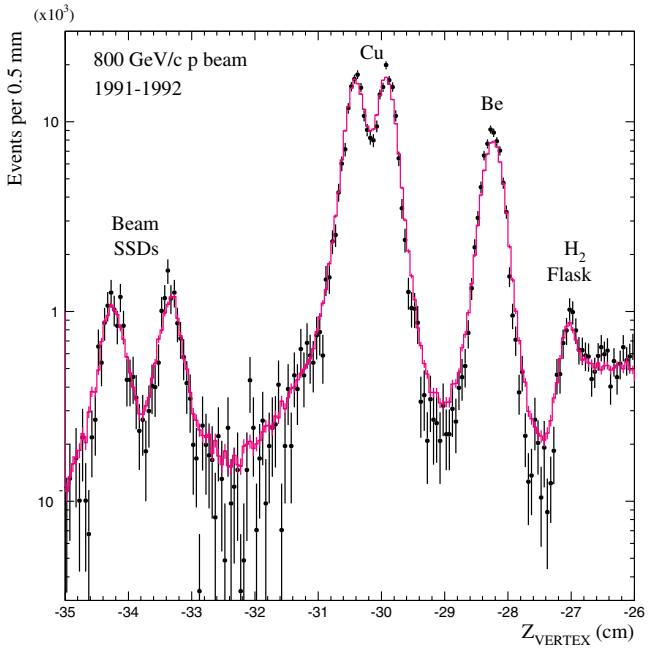

FIG. 10 (color online). Z positions of primary vertices in the vicinity of the Cu targets in the detailed Monte Carlo simulation (•) and the data (histogram), for events containing π^0 candidates with $p_T > 4.0$ GeV/c in the 800 GeV/c sample. Note the use of logarithmic scale.

Longitudinal positions were determined using Monte Carlo methods based upon the interaction lengths of the materials in the target region (Table I). DGS events were weighted to reproduce the relative number of vertices in the data. Results from the DGS compare favorably with the data in Fig. 8. This good agreement was particularly important for separating events with primary vertices in copper from those in the upstream piece of beryllium. Figure 10 displays the longitudinal vertex distribution, focusing on this region in the 1991–1992 target configuration. The shapes of the tails in the data are well described by the DGS.

The vertex reconstruction efficiency was evaluated using the DGS [31]. Separate reconstruction efficiencies were evaluated for the Be, Cu, and H_2 targets. The reconstruction probability was defined as the number of vertices reconstructed in each target's fiducial volume divided by the number of vertices generated in the fiducial volume. The reconstruction efficiency was the inverse of this probability. Defined in this manner, the reconstruction efficiency also corrected for the longitudinal resolution smearing of reconstructed vertices.

Additional beam particles occasionally interacted in the target material within the data-capture timing window of the tracking system. The extra tracks sometimes caused the vertex associated with the high-p_T interaction to be misidentified. The bias introduced by these rare events favored configurations where the low-p_T interaction took place within the downstream piece of Be. This primarily affected interactions in the Cu and upstream Be targets in the long 1991–1992 target configuration because of the relatively poor vertex resolution in those targets compared to the downstream Be. This bias was investigated by comparing the π^0 cross sections measured in π^-Be interactions in the 1990 and the 1991–1992 runs, and by comparing π^0 yields from the upstream and downstream Be pieces in the 1991–1992 target configuration. The number of Cu vertices were corrected for misidentifications arising from this source. The resulting correction was 1.04 for the 1991–1992 π^-Cu sample at 515 GeV/c, 1.06 for the 530 GeV/c pCu sample, and 1.12 for the 800 GeV/c pCu sample [35].

Each event in this analysis was required to have a reconstructed vertex in the target region. Longitudinal and transverse requirements were placed on vertices to define the data samples. The longitudinal cuts selected the target in which the incident beam interacted, while the transverse cuts ensured that the interaction occurred within the target material.

F. Direct photons

The largest contribution to the direct-photon background comes from electromagnetic decays of neutral hadrons, particularly π^0's and η's. For the purposes of the measurements reported here, a photon was a direct-photon candidate if it did not combine with another photon in the same octant to form a π^0 with $A_{\gamma\gamma} \leq 0.9$ or an η with $A_{\gamma\gamma} \leq 0.8$.

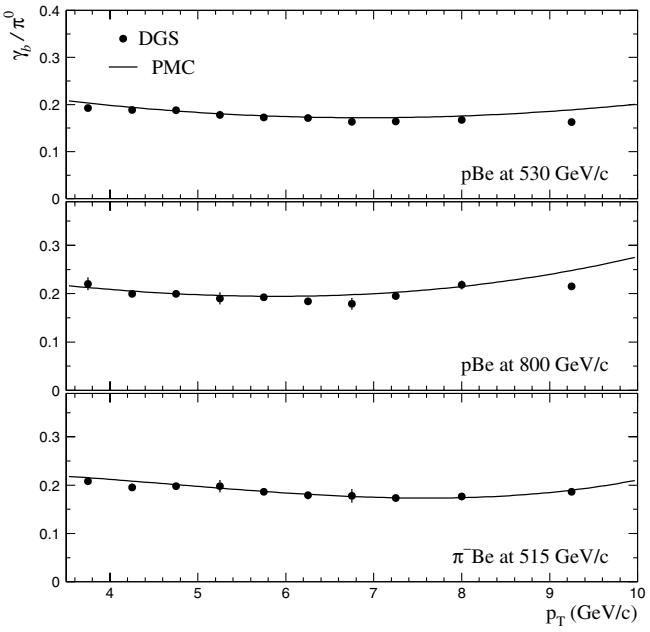

FIG. 11. A comparison of the direct-photon background as a function of p_T as predicted by the parameterized Monte Carlo simulation (line) and the detailed Monte Carlo simulation (•). The background was normalized to the π^0 cross section.

To suppress electrons, reconstructed showers were excluded from the sample when charged-particle tracks pointed to within 1 cm of shower center. The correction for this criterion in the direct-photon analysis is ≈ 1.01 based upon studies of the impact of this requirement on reconstructed π^0's.

The residual background from π^0's and η's, as well as from other sources of background, was calculated using DGS samples that contained no generated direct photons (γ_b). A smooth fit of the γ_b/π^0 in p_T and rapidity was used

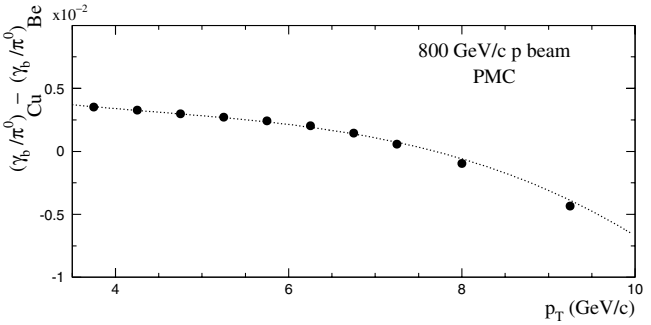

FIG. 12. Difference between the copper and beryllium background γ/π^0 ratios versus p_T for the 800 GeV/c proton beam. The dotted line represents a fit to the difference integrated over rapidity.

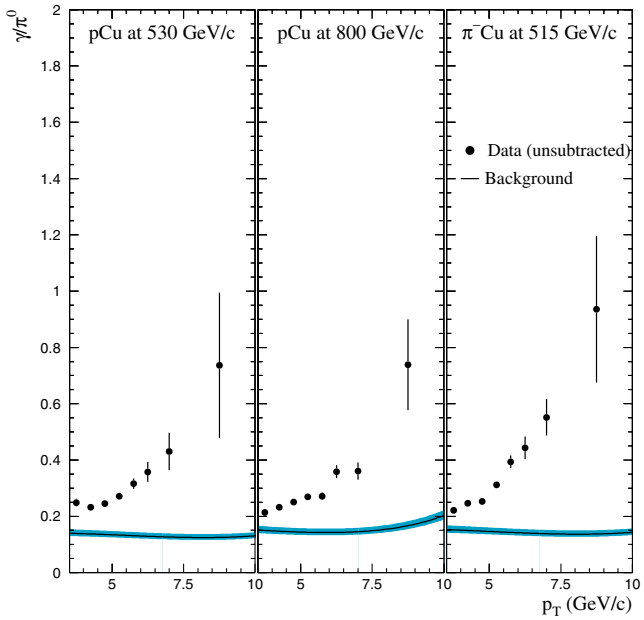

FIG. 13 (color online). γ/π^0 ratio for each of the three beam samples as a function of p_T. Direct-photon candidates in the data are indicated by the points. The error bars represent statistical contributions to the uncertainties. The line indicates the expected background and its width is representative of the associated systematic uncertainty.

to extract the direct-photon cross sections. The systematic uncertainty in this background subtraction was estimated by varying the direct-photon definition as a function of the cut on $A_{\gamma\gamma}$. The direct-photon background was also investigated using the PMC. Figure 11 compares the direct-photon backgrounds estimated using the two Monte Carlo simulations. The close agreement provides additional confidence in our understanding of the background in our direct-photon samples. Additional details are provided in Ref. [17].

Fits to γ_b/π^0 were only made for the beryllium target due to relatively poor DGS statistics in the other targets. However, γ_b/π^0 is expected to be slightly different for each target due to the different amounts of target material the photons must traverse. Therefore, a correction to γ_b/π^0 was calculated using the PMC. The differences in γ_b/π^0 are shown for the 800 GeV/c proton beam data in Fig. 12. The other data samples have similar behavior. The target differences were fit as functions of p_T and rapidity for each incident beam and target configuration and applied as additive corrections to the nominal γ_b/π^0 fit.

The impact of the background can be determined by normalizing the direct-photon candidate spectrum from the data and the simulation to the measured π^0 cross section [15,16]. This γ/π^0 ratio is displayed in Fig. 13 for all three incident beams for the copper target. The signal-to-background in all cases is large at high p_T.

G. Summary of systematic uncertainties

The systematic uncertainties for the production of π^0's, η's, and direct photons measured in π^-Cu and pCu interactions are similar to those detailed in Refs. [15–17]. The principal contributions to the systematic uncertainty arose from the following sources: normalization, calibration of photon energy response and detector-resolution unsmearing, background subtraction, reconstruction efficiency, incident beam contamination (for the 515 GeV/c and 530 GeV/c secondary beams), beam-halo muon rejection, geometric acceptance, photon conversions, trigger response, and vertex finding. The additional vertex-finding uncertainty associated with the confusion induced by multiple beam particles interacting in the target was $\approx 2\%$. The total systematic uncertainties, combined in quadrature, are quoted with the cross sections in the appropriate tables. Note that some of these contributions to the systematic uncertainty (e.g. normalization) are strongly correlated between bins.

Most of the experimental systematic uncertainties cancel in the ratio of cross sections measured on different targets. The residual uncertainties are due to target-related systematics associated mainly with vertex identification. The total systematic uncertainty in the ratio of cross sections measured on Cu to those on Be is $\pm 3\%$ for the 800 GeV/c p beam sample, and $\pm 2\%$ for the 530 GeV/c p and 515 GeV/c π^- beam samples. The

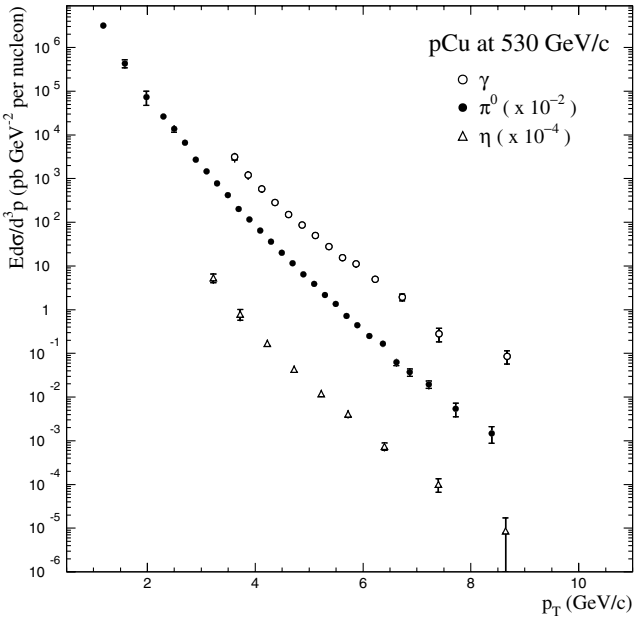

FIG. 14. Invariant differential cross sections per nucleon for direct-photon, π^0, and η production as functions of p_T, averaged over $-0.75 \leq y_{\rm cm} \leq 0.75$, from 530 GeV/$c$ proton beam incident upon a copper target. The π^0 and η cross sections have been scaled relative to the photon cross sections, and each other, to prevent the data points from overlapping.

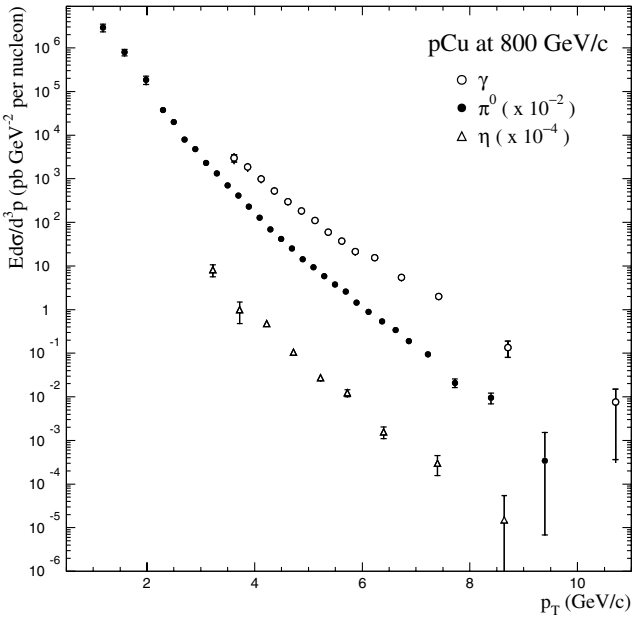

FIG. 15. Invariant differential cross sections per nucleon for direct-photon, π^0, and η production as functions of p_T, averaged over $-1.0 \leq y_{\rm cm} \leq 0.5$, from 800 GeV/$c$ proton beam incident upon a copper target. The π^0 and η cross sections have been scaled relative to the photon cross sections, and each other, to prevent the data points from overlapping.

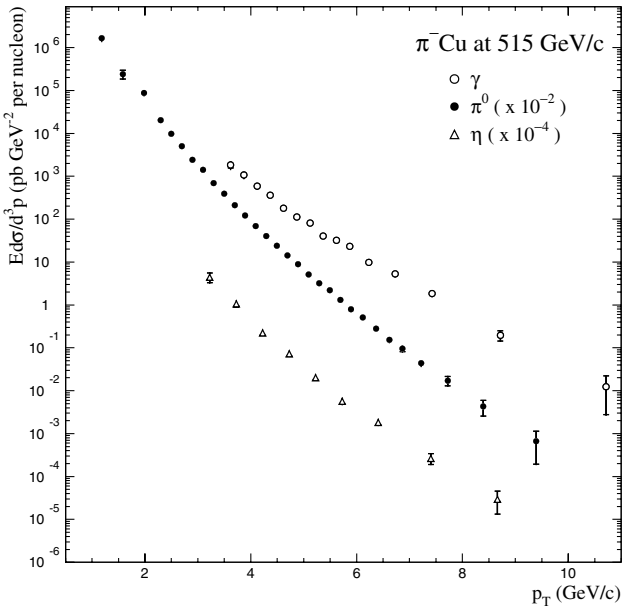

FIG. 16. Invariant differential cross sections per nucleon for direct-photon, π^0, and η production as functions of p_T, averaged over $-0.75 \leq y_{\rm cm} \leq 0.75$, for 515 GeV/$c$ π^- beam incident upon a copper target. The π^0 and η cross sections have been scaled relative to the photon cross sections, and each other, to prevent the data points from overlapping.

systematic uncertainty associated with the ratios of Be to H and Cu to H are $\pm 4\%$ for all samples after correcting for the effects of vertex misidentification as discussed in Sec. III E.

IV. RESULTS AND DISCUSSION

A. Cross sections

The invariant differential cross sections per nucleon for direct-photon, π^0, and η production from 530 and 800 GeV/c p beams and 515 GeV/c π^- beam incident on copper are presented as functions of p_T in Figs. 14–16. Results from 530 GeV/c p and 515 GeV/c π^- beams are averaged over the beam-nucleon center-of-mass rapidity range $-0.75 \leq y_{\rm cm} \leq 0.75$; results from the 800 GeV/c p beam are averaged over $-1.0 \leq y_{\rm cm} \leq 0.5$. Data points are plotted at abscissa values that correspond to the average value of the cross section in each p_T bin, assuming local exponential p_T dependence [36]. The inclusive cross sections are tabulated in Tables III, IV, and V of the appendix.

B. Ratios

E706 has previously reported results for direct-photon and π^0 production on beryllium and hydrogen targets [15–17]. Since E706 is the only direct-photon experiment that

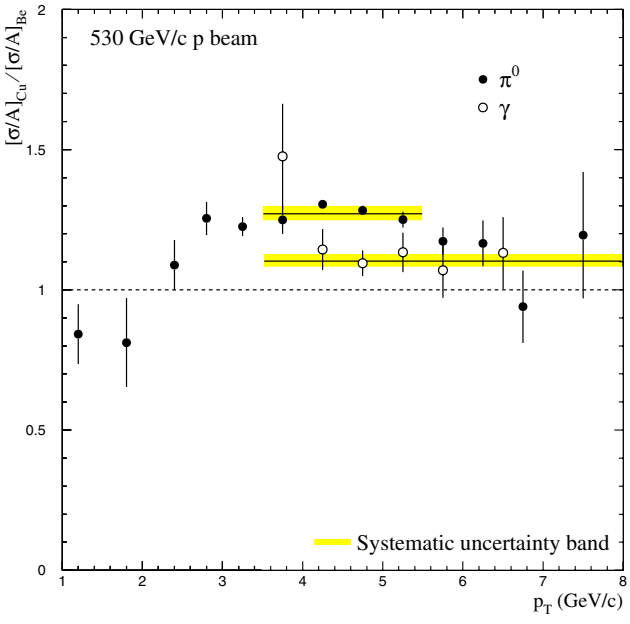

FIG. 17 (color online). The ratio of inclusive π^0 and direct-photon production cross sections per nucleon in pCu to those in pBe collisions at 530 GeV/c. Simple straight line fits to regions with relatively flat distributions have been overlaid on the data. The error bars represent only statistical contributions to the uncertainties. Systematic uncertainties are indicated by the shaded region associated with the fit.

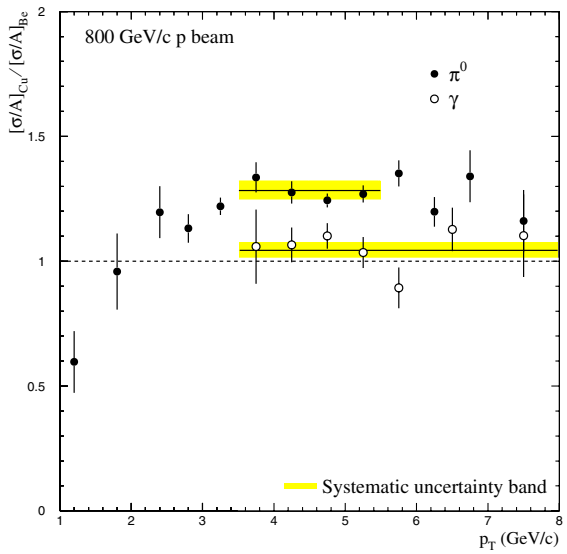

FIG. 18 (color online). The ratio of inclusive π^0 and direct-photon production cross sections per nucleon in pCu to those in pBe collisions at 800 GeV/c. Simple straight line fits to regions with relatively flat distributions have been overlaid on the data. The error bars represent only statistical contributions to the uncertainties. Systematic uncertainties are indicated by the shaded region associated with the fit.

TABLE II. Results of fits of the Cu to Be ratios for π^0 and direct-photon production.

Sample	π^0 $3.5 < p_T < 5.5$ GeV/c	Direct photon $3.5 < p_T < 8.0$ GeV/c
530 GeV/c p	$1.271 \pm 0.016 \pm 0.025$	$1.103 \pm 0.032 \pm 0.022$
800 GeV/c p	$1.283 \pm 0.025 \pm 0.038$	$1.043 \pm 0.032 \pm 0.031$
515 GeV/c π^-	$1.237 \pm 0.015 \pm 0.025$	$1.083 \pm 0.024 \pm 0.022$

used more than one nuclear target, our data provide a unique measurement of nuclear effects in direct-photon production. Figures 17–19 present the ratio of inclusive cross sections per nucleon measured on Cu to those measured on Be for π^0 mesons and direct photons. (The Be/H ratios were presented in previous publications [15–17], and are not reproduced here.) These ratios show clear evidence of nuclear enhancement in both π^0 and direct-photon production and the π^0 data exhibit the decrease at high p_T first noted by Cronin *et al.* [6,7]. This behavior is generally attributed to the influence of multiple-parton scattering prior to the hard scatter [37].

Results from fits to constant ratios in restricted regions of p_T have been overlaid on the data in Figs. 17–19, and summarized in Table II. Fits were made for $3.5 < p_T < 5.5$ GeV/c for the π^0's and over the entire p_T range for the

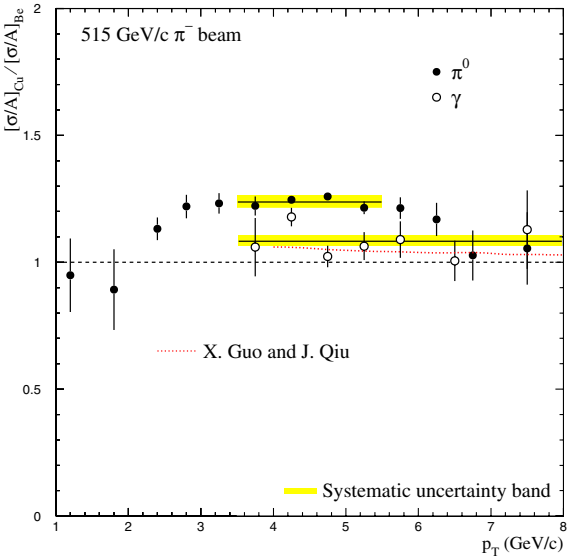

FIG. 19 (color online). The ratio of inclusive π^0 and direct-photon production cross sections per nucleon in π^-Cu to those in π^-Be collisions at 515 GeV/c. A theoretical prediction for direct-photon production from Guo and Qiu [38] is overlaid on the data (dotted curve). Simple straight line fits to regions with relatively flat distributions have also been overlaid on the data. The error bars represent only statistical contributions to the uncertainties. Systematic uncertainties are indicated by the shaded region associated with the fit.

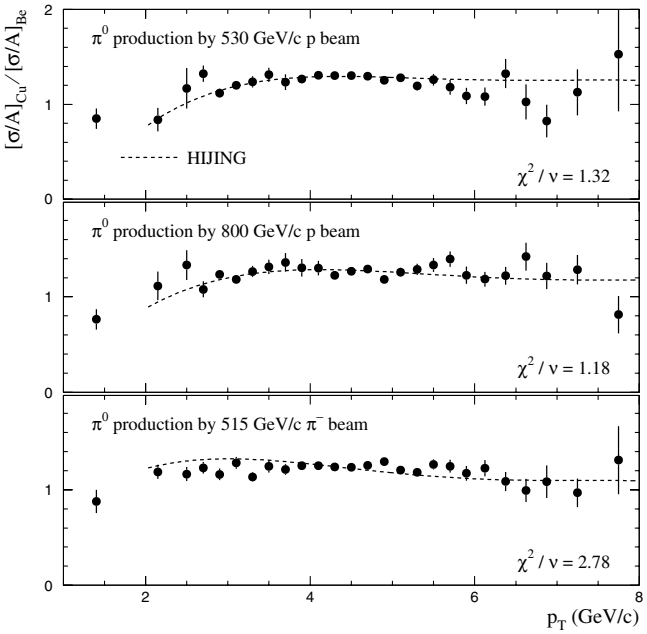

FIG. 20. The ratio of inclusive π^0 production cross sections per nucleon on Cu to those on Be, compared with predictions from HIJING scaled to the data. The error bars represent only statistical contributions to the uncertainties and ν represents the number of degrees of freedom of the fit.

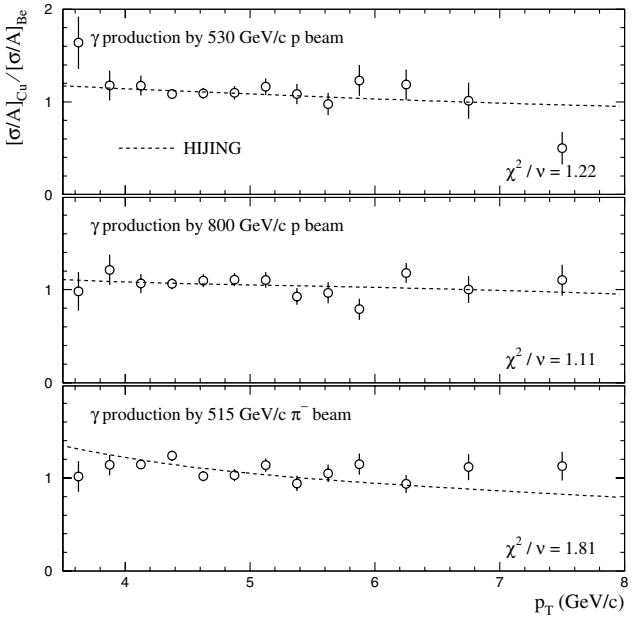

FIG. 21. The ratio of inclusive direct-photon production cross sections per nucleon on Cu to those on Be, compared with predictions from HIJING scaled to the data. The error bars represent only statistical contributions to the uncertainties and ν represents the number of degrees of freedom of the fit.

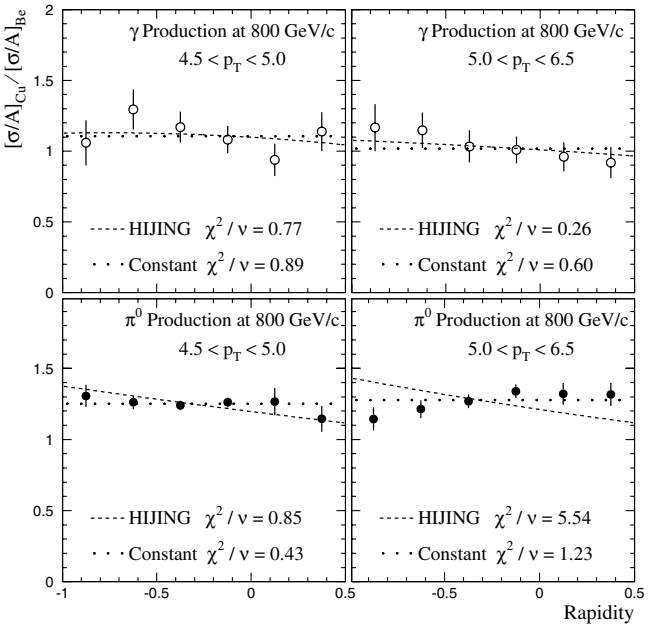

FIG. 23. The rapidity dependence of the ratio of inclusive cross sections per nucleon on Cu to those on Be for direct-photon and π^0 production in the 800 GeV/c p beam, compared with predictions from HIJING scaled to the data. The error bars represent only statistical contributions to the uncertainties and ν represents the number of degrees of freedom of the fit.

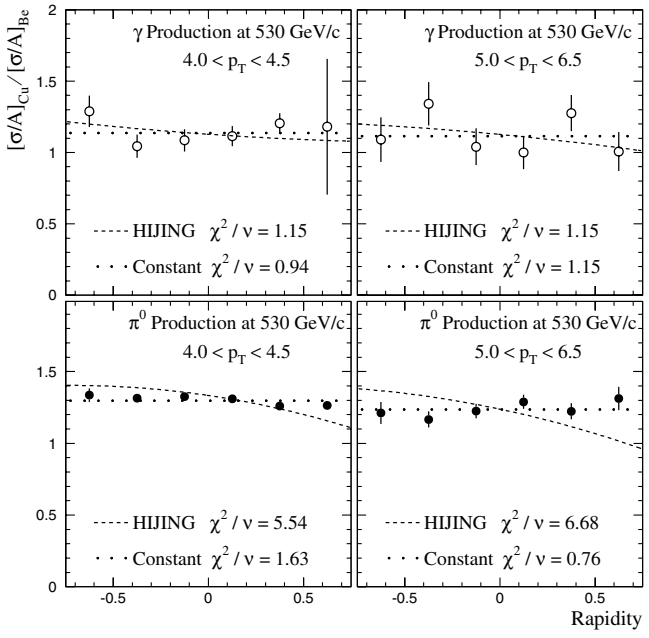

FIG. 22. The rapidity dependence of the ratio of inclusive cross sections per nucleon on Cu to those on Be for direct-photon and π^0 production in the 530 GeV/c p beam, compared with predictions from HIJING scaled to the data. The error bars represent only statistical contributions to the uncertainties and ν represents the number of degrees of freedom of the fit.

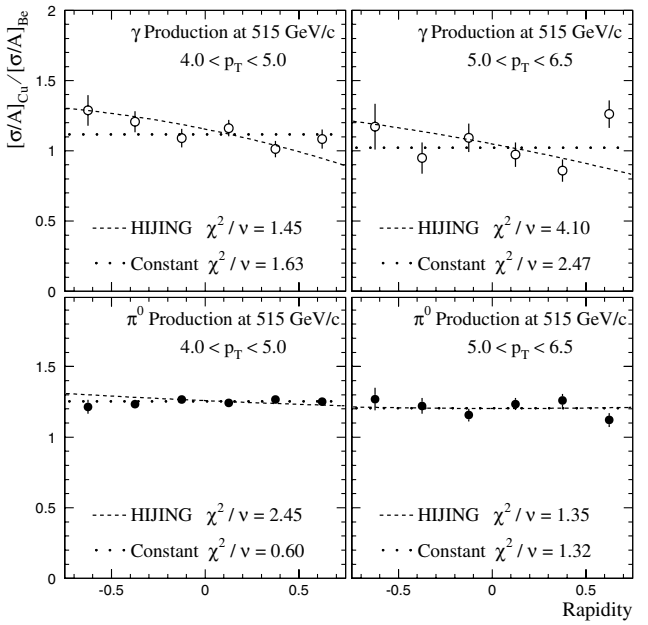

FIG. 24. The rapidity dependence of the ratio of inclusive cross sections per nucleon on Cu to those on Be for direct-photon and π^0 production in the 515 GeV/c π^- beam, compared with predictions from HIJING scaled to the data. The error bars represent only statistical contributions to the uncertainties and ν represents the number of degrees of freedom of the fit.

direct photons. The difference in the ratio for π^0 mesons and direct photons is significant and may be indicative of differing roles of initial and final-state effects, since direct photons are not expected to be strongly impacted by final-state nuclear effects.

Expectations from a theoretical prediction for nuclear enhancement in the 515 GeV/c π^- direct-photon sample [38] have been overlaid on Fig. 19. This calculation predicts a slight enhancement in direct-photon production and agrees with the data within the uncertainties.

C. Comparisons with HIJING

Figures 20 and 21 compare the ratio of the Cu and Be cross sections, for pizero and direct-photon production, respectively, to results obtained from version 1.381 of the HIJING Monte Carlo. The direct output from HIJING, an event generator designed to simulate particle production in pp, pA, and AA collisions [13], has been normalized to the data in producing these figures [39]. For the proton beams, the shapes of the HIJING curves are observed to be in good agreement with the data.

Renewed interest in the amount of nuclear enhancement as a function of rapidity has been generated by recent BRAHMS measurements [40] and corresponding results from the other RHIC experiments [9–11]. Our high-statistics cross-section measurements in the central rapidity region can be used to tune theoretical models developed to describe the RHIC environment. The rapidity dependence of the Cu to Be cross-section ratios are compared to expectations from HIJING in Figs. 22–24. HIJING does not describe the rapidity dependence of the π^0 data for the incident proton beams; the HIJING results are generally peaked towards backward rapidities (like the BRAHMS data), whereas our data are relatively independent of rapidity. HIJING provides a better description of our direct-photon data.

V. CONCLUSIONS

We have measured the invariant differential cross section per nucleon for direct-photon, π^0, and η production from 515 GeV/c π^- beam and 800 and 530 GeV/c proton beams incident on copper as a function of p_T and $y_{\rm cm}$. These data span the kinematic range $1.0 < p_T \lesssim 10$ GeV/c and central rapidities.

Ratios of these production cross sections to our previously published measurements on a beryllium target [15–17] show a strong nuclear enhancement for π^0 mesons and a smaller, but significant, enhancement for direct photons. We compare these measurements with expectations from a theoretical calculation (for direct-photon production for incident π^- beam) and with the results of a Monte Carlo event generator, HIJING, dedicated to the simulation of nuclear effects. HIJING yields a good description of the shape of the p_T dependence of the Cu to Be ratios for both π^0's and direct photons in the incident proton beam data samples. HIJING also describes the rapidity dependence of direct-photon production in those samples. However, HIJING provides a relatively poor description of the rapidity dependence of π^0 meson production.

ACKNOWLEDGMENTS

We thank the U.S. Department of Energy, the National Science Foundation, including its Office of International Programs, and the Universities Grants Commission of India, for their support of this research. The staff and management of Fermilab are thanked for their efforts in making available the beam and computing facilities that made this work possible. We are pleased to acknowledge the contributions of our colleagues on Fermilab experiment E672. We acknowledge the contributions of the following colleagues to the operation and upgrade of the Meson West spectrometer: W. Dickerson and E. Pothier from Northeastern University; J. T. Anderson, E. Barsotti, Jr., H. Koecher, P. Madsen, D. Petravick, R. Tokarek, J. Tweed, D. Allspach, J. Urbin, and the cryo crews from Fermi National Accelerator Laboratory; T. Haelen, C. Benson, L. Kuntz, and D. Ruggiero from the University of Rochester; the technical staffs of Michigan State University and Pennsylvania State University for the construction of the straw tubes and of the University of Pittsburgh for the silicon detectors. We thank the following commissioning run collaborators for their invaluable contributions to the hardware and software infrastructure of the original Meson West spectrometer: G. Alverson, G. Ballocchi, R. Benson, D. Berg, D. Brown, D. Carey, T. Chand, C. Chandlee, S. Easo, W. Faissler, G. Glass, I. Kourbanis, A. Lanaro, C. Nelson, Jr., D. Orris, B. Rajaram, K. Ruddick, A. Sinanidis, and G. Wu. We also thank X.-N. Wang for several helpful discussions.

APPENDIX: TABULATED CROSS SECTIONS

In this appendix, we present tables of the measured invariant differential cross sections for direct-photon, π^0, and η production on Cu targets as functions of p_T. In these tables, the first uncertainty is statistical and the second is systematic. In the case of the lowest two p_T bins for the π^0 measurement, the statistical and systematic uncertainties have been combined because of the large correlation between them.

TABLE III. Invariant differential cross sections ($Ed\sigma/d^3p$) per nucleon for direct-photon production in pCu collisions at 800 and 530 GeV/c, and π^-Cu collisions at 515 GeV/c as functions of p_T.

p_T (GeV/c)	pCu at 530 GeV/c $-0.75 \le y_{cm} \le 0.75$ [nb/(GeV/c)^2]	pCu at 800 GeV/c $-1.0 \le y_{cm} \le 0.5$ [nb/(GeV/c)^2]	π^-Cu at515 GeV/c $-0.75 \le y_{cm} \le 0.75$ [nb/(GeV/c)^2]
3.50–3.75	3.11 ± 0.45 ± 0.63	3.01 ± 0.59 ± 0.63	1.84 ± 0.28 ± 0.34
3.75–4.00	1.21 ± 0.15 ± 0.22	1.87 ± 0.23 ± 0.36	1.065 ± 0.095 ± 0.18
4.00–4.25	0.583 ± 0.048 ± 0.099	0.989 ± 0.089 ± 0.17	0.585 ± 0.022 ± 0.093
4.25–4.50	0.282 ± 0.011 ± 0.045	0.523 ± 0.026 ± 0.086	0.361 ± 0.015 ± 0.053
4.50–4.75	0.1516 ± 0.0074 ± 0.023	0.299 ± 0.017 ± 0.046	0.1783 ± 0.0092 ± 0.025
4.75–5.00	0.0865 ± 0.0052 ± 0.012	0.182 ± 0.011 ± 0.026	0.1124 ± 0.0066 ± 0.015
	[pb/(GeV/c)^2]	[pb/(GeV/c)^2]	[pb/(GeV/c)^2]
5.00–5.25	50.2 ± 3.5 ± 6.7	110.6 ± 7.6 ± 15	81.0 ± 4.8 ± 10
5.25–5.50	27.7 ± 2.5 ± 3.6	59.9 ± 5.5 ± 7.9	40.4 ± 3.4 ± 4.9
5.50–5.75	15.6 ± 1.8 ± 2.0	37.0 ± 4.1 ± 4.7	32.3 ± 2.7 ± 3.9
5.75–6.00	11.2 ± 1.3 ± 1.4	21.4 ± 2.9 ± 2.7	23.1 ± 2.1 ± 2.7
6.00–6.50	4.99 ± 0.62 ± 0.61	15.4 ± 1.3 ± 1.9	9.74 ± 0.95 ± 1.1
6.50–7.00	1.93 ± 0.34 ± 0.24	5.43 ± 0.72 ± 0.64	5.30 ± 0.60 ± 0.61
7.00–8.00	0.278 ± 0.094 ± 0.035	2.01 ± 0.27 ± 0.23	1.84 ± 0.23 ± 0.22
8.00–10.00	0.086 ± 0.029 ± 0.012	0.136 ± 0.055 ± 0.016	0.197 ± 0.052 ± 0.024
10.00–12.00		0.0077 ± 0.0077 ± 0.0009	0.0124 ± 0.0097 ± 0.0016

TABLE IV. Invariant differential cross sections ($Ed\sigma/d^3p$) per nucleon for π^0 production in pCu collisions at 800 and 530 GeV/c, and π^-Cu collisions at 515 GeV/c as functions of p_T.

p_T (GeV/c)	pCu at 530 GeV/c $-0.75 \le y_{cm} \le 0.75$ [μb/(GeV/c)^2]	pCu at 800 GeV/c $-1.0 \le y_{cm} \le 0.5$ [μb/(GeV/c)^2]	π^-Cu at 515 GeV/c $-0.75 \le y_{cm} \le 0.75$ [μb/(GeV/c)^2]
1.00–1.40	315 ± 50	293 ± 67	166 ± 32
1.40–1.80	43.2 ± 9.9	79 ± 16	23.9 ± 6.2
1.80–2.20	7.3 ± 2.6 ± 0.8	18.5 ± 4.1 ± 2.0	8.72 ± 0.88 ± 1.0
2.20–2.40	2.64 ± 0.19 ± 0.28	3.77 ± 0.40 ± 0.42	2.015 ± 0.094 ± 0.24
2.40–2.60	1.38 ± 0.23 ± 0.15	2.00 ± 0.20 ± 0.22	0.973 ± 0.057 ± 0.11
2.60–2.80	0.663 ± 0.041 ± 0.070	0.797 ± 0.053 ± 0.088	0.505 ± 0.023 ± 0.058
2.80–3.00	0.2723 ± 0.0093 ± 0.029	0.476 ± 0.014 ± 0.052	0.244 ± 0.012 ± 0.028
3.00–3.20	0.1453 ± 0.0048 ± 0.016	0.2287 ± 0.0082 ± 0.025	0.1417 ± 0.0062 ± 0.016
	[nb/(GeV/c)^2]	[nb/(GeV/c)^2]	[nb/(GeV/c)^2]
3.20–3.40	77.5 ± 3.2 ± 8.2	132.5 ± 5.3 ± 15	69.2 ± 2.7 ± 7.7
3.40–3.60	42.0 ± 2.1 ± 4.5	70.1 ± 3.5 ± 7.7	39.1 ± 2.0 ± 4.3
3.60–3.80	20.0 ± 1.2 ± 2.1	41.2 ± 2.6 ± 4.5	21.20 ± 0.92 ± 2.4
3.80–4.00	11.53 ± 0.34 ± 1.2	23.1 ± 1.4 ± 2.5	12.27 ± 0.37 ± 1.4
4.00–4.20	6.411 ± 0.067 ± 0.69	12.74 ± 0.68 ± 1.4	6.947 ± 0.075 ± 0.77
4.20–4.40	3.579 ± 0.043 ± 0.39	6.89 ± 0.15 ± 0.76	4.021 ± 0.054 ± 0.44
4.40–4.60	2.002 ± 0.030 ± 0.22	4.15 ± 0.12 ± 0.46	2.389 ± 0.035 ± 0.26
4.60–4.80	1.146 ± 0.020 ± 0.13	2.528 ± 0.075 ± 0.28	1.438 ± 0.024 ± 0.16
4.80–5.00	0.639 ± 0.014 ± 0.070	1.426 ± 0.041 ± 0.16	0.892 ± 0.018 ± 0.098
	[pb/(GeV/c)^2]	[pb/(GeV/c)^2]	[pb/(GeV/c)^2]
5.00–5.20	392 ± 11 ± 43	931 ± 31 ± 110	514 ± 13 ± 57
5.20–5.40	215.8 ± 7.6 ± 24	582 ± 23 ± 66	320 ± 11 ± 35
5.40–5.60	134.3 ± 5.9 ± 15	374 ± 18 ± 42	219.2 ± 8.3 ± 24
5.60–5.80	72.2 ± 4.3 ± 8.1	258 ± 14 ± 29	130.9 ± 6.7 ± 15
5.80–6.00	44.4 ± 3.2 ± 5.0	143.6 ± 9.3 ± 16	79.7 ± 4.7 ± 8.9
6.00–6.25	25.2 ± 2.0 ± 2.9	88.7 ± 5.2 ± 10	51.2 ± 3.3 ± 5.8
6.25–6.50	16.6 ± 1.7 ± 1.9	53.9 ± 3.7 ± 6.3	27.8 ± 2.4 ± 3.2
6.50–6.75	6.3 ± 1.0 ± 0.7	33.8 ± 3.1 ± 3.9	15.3 ± 1.7 ± 1.7
6.75–7.00	3.71 ± 0.71 ± 0.44	19.1 ± 1.9 ± 2.2	9.5 ± 1.4 ± 1.1
7.00–7.50	1.96 ± 0.38 ± 0.23	9.5 ± 1.0 ± 1.1	4.39 ± 0.63 ± 0.51
7.50–8.00	0.54 ± 0.18 ± 0.07	2.10 ± 0.46 ± 0.25	1.73 ± 0.44 ± 0.21
8.00–9.00	0.149 ± 0.061 ± 0.019	0.95 ± 0.26 ± 0.12	0.43 ± 0.17 ± 0.05
9.00–10.00			0.067 ± 0.047 ± 0.009

TABLE V. Invariant differential cross sections ($Ed\sigma/d^3p$) per nucleon for η production in pCu collisions at 800 and 530 GeV/c, and π^-Cu collisions at 515 GeV/c as functions of p_T.

p_T (GeV/c)	pCu at 530 GeV/c $-0.75 \le y_{cm} \le 0.75$ [nb/(GeV/c)^2]	pCu at 800 GeV/c $-1.0 \le y_{cm} \le 0.5$ [nb/(GeV/c)^2]	π^-Cu at 515 GeV/c $-0.75 \le y_{cm} \le 0.75$ [nb/(GeV/c)^2]
3.00–3.50	$53 \pm 12 \pm 6.0$	$82 \pm 25 \pm 10$	$44 \pm 12 \pm 6.0$
3.50–4.00	$7.9 \pm 2.2 \pm 0.9$	$9.9 \pm 5.1 \pm 1.2$	$10.6 \pm 1.6 \pm 1.3$
4.00–4.50	$1.68 \pm 0.17 \pm 0.19$	$4.78 \pm 0.47 \pm 0.56$	$2.21 \pm 0.17 \pm 0.26$
4.50–5.00	$0.434 \pm 0.043 \pm 0.050$	$1.06 \pm 0.12 \pm 0.12$	$0.730 \pm 0.049 \pm 0.084$
	[pb/(GeV/c)^2]	[pb/(GeV/c)^2]	[pb/(GeV/c)^2]
5.00–5.50	$120 \pm 13 \pm 14$	$274 \pm 37 \pm 32$	$203 \pm 17 \pm 24$
5.50–6.00	$41.0 \pm 6.6 \pm 4.9$	$123 \pm 23 \pm 15$	$56.6 \pm 8.0 \pm 6.6$
6.00–7.00	$7.5 \pm 1.4 \pm 0.9$	$15.8 \pm 4.7 \pm 1.9$	$18.2 \pm 2.3 \pm 2.2$
7.00–8.00	$1.01 \pm 0.35 \pm 0.13$	$3.0 \pm 1.5 \pm 0.4$	$2.66 \pm 0.76 \pm 0.33$
8.00–10.00	$0.087 \pm 0.084 \pm 0.012$	$0.15 \pm 0.41 \pm 0.02$	$0.29 \pm 0.16 \pm 0.04$

[1] W. M. Geist *et al.*, Phys. Rep. **197**, 263 (1990).
[2] N. A. McCubbin, Rep. Prog. Phys. **44**, 1027 (1981).
[3] J. F. Owens, Rev. Mod. Phys. **59**, 465 (1987).
[4] T. Ferbel and W. R. Molzon, Rev. Mod. Phys. **56**, 181 (1984).
[5] L. Apanasevich *et al.*, Phys. Rev. D **59**, 074007 (1999).
[6] J. W. Cronin *et al.*, Phys. Rev. D **11**, 3105 (1975).
[7] D. Antreasyan *et al.*, Phys. Rev. D **19**, 764 (1979).
[8] H. Frisch *et al.*, Phys. Rev. D **27**, 1001 (1983).
[9] J. Adams *et al.* (STAR Collaboration), Nucl. Phys. **A757**, 102 (2005).
[10] K. Adcox *et al.* (PHENIX Collaboration), Nucl. Phys. **A757**, 184 (2005).
[11] B. B. Back *et al.* (PHOBOS Collaboration), Nucl. Phys. **A757**, 28 (2005).
[12] I. Arsene *et al.* (BRAHMS Collaboration), Nucl. Phys. **A757**, 1 (2005).
[13] X.-N. Wang, Nucl. Phys. **A661**, 609 (1999), and private communication with the author regarding the use of HIJING at our beam energies and for π^- beams.
[14] L. Apanasevich *et al.* (E706 Collaboration), Phys. Rev. Lett. **81**, 2642 (1998).
[15] L. Apanasevich *et al.* (E706 Collaboration), Phys. Rev. D **68**, 052001 (2003). A computational error in the correction of measured cross sections for contributions from minority particles in secondary beams affected the reported cross sections for π^0 and η production by 530 GeV/c protons. As a result, the cross sections listed in the tables for 530 GeV/c protons in the referenced publication should be increased by 3.4%, a change that falls well within the quoted systematic uncertainties.
[16] L. Apanasevich *et al.* (E706 Collaboration), Phys. Rev. D **69**, 032003 (2004).
[17] L. Apanasevich *et al.* (E706 Collaboration), Phys. Rev. D **70**, 092009 (2004).
[18] L. Apanasevich *et al.* (E706 Collaboration), Phys. Rev. D **56**, 1391 (1997).
[19] L. Apanasevich *et al.* (E706 Collaboration), hep-ex/0004012.
[20] L. Apanasevich *et al.* (E706 Collaboration), Nucl. Instrum. Methods Phys. Res., Sect. A **417**, 50 (1998).
[21] D. Allspach *et al.*, in *Advances in Cryogenic Engineering*, edited by R. W. Fast (Plenum, New York, 1991), Vol. 37, p. 1495.
[22] A. S. Carroll *et al.*, Phys. Lett. **80B**, 319 (1979).
[23] A. Baldini *et al.*, in *Total Cross-Sections for Reactions of High Energy Particles*, edited by H. Schopper (Springer-Verlag, New York, 1988), Vol. 12.
[24] C. Bromberg *et al.* (E706 Collaboration), Nucl. Instrum. Methods Phys. Res., Sect. A **307**, 292 (1991).
[25] D. Striley, Ph.D. thesis, University of Missouri at Columbia, 1996.
[26] L. Sorrell, E706 Note 201, 1994 (unpublished); Ph.D. thesis, Michigan State University, 1995; G. Osborne, Ph.D. thesis, University of Rochester, 1996.
[27] During the 1990 run, the beam hole definition was implemented using a single scintillation counter. An array of four scintillation counters was used for the beam hole definition during the 1991–1992 run.
[28] S. Blusk, Ph.D. thesis, University of Pittsburgh, 1995.
[29] D. E. Groom *et al.* (Particle Data Group), Eur. Phys. J. C **15**, 1 (2000).
[30] F. Carminati *et al.*, CERN Program Library Long Writeup W5013, 1993.
[31] L. Apanasevich, Ph.D. thesis, Michigan State University, 2005.
[32] G. Marchesini *et al.*, Comput. Phys. Commun. **67**, 465 (1992), HERWIG v5.6.
[33] M. Begel, Ph.D. thesis, University of Rochester, 1999.
[34] M. Diakonou *et al.* (R806 Collaboration), Phys. Lett. **89B**, 432 (1980).
[35] Our previously published cross sections on hydrogen were not corrected for these misidentified vertices (the corresponding corrections in the case of Be were negligible). The applicable correction factors are 1.01 for the 1991–1992 $\pi^- p$ sample at 515 GeV/c, 1.02 for the 530 GeV/c pp sample, and 1.06 for the 800 GeV/c pp sample. In each case, the additional correction falls within our published systematic uncertainty.
[36] G. D. Lafferty and T. R. Wyatt, Nucl. Instrum. Methods Phys. Res., Sect. A **355**, 541 (1995).
[37] X.-N. Wang, Phys. Rep. **280**, 287 (1997).
[38] X. Guo and J. Qiu, Phys. Rev. D **53**, 6144 (1996).
[39] The normalization factors applied to the HIJING results before comparing them to our data were 1.27, 1.34, and 1.46 in Fig. 20 and 1.27, 1.15, and 1.70 in Fig. 21, listing

from top to bottom in each case. In addition to requiring overall rescaling, the HIJING results varied depending on the p_T threshold employed in the generation. These effects were only a few percent for high p_T thresholds ($p_T^{\min} > 5.0$ GeV$/c$), but were as large as 30%–50% for $p_T^{\min} < 3.0$ GeV$/c$. We corrected for this threshold dependence by normalizing all generated samples, for a particular beam and produced particle, to the one with the highest p_T threshold.

[40] I. Arsene *et al.* (BRAHMS Collaboration), Phys. Rev. Lett. **93**, 242303 (2004).